# Nanoscale

## PAPER

Check for updates

# Shape-dependent thermo-plasmonic effect of nanoporous gold at the nanoscale for ultrasensitive heat-mediated remote actuation†

Zhe Yang,‡[a] Xuemei Han,‡[a] Hiang Kwee Lee,‡[a,b] Gia Chuong Phan-Quang,[a] Charlynn Sher Lin Koh,[a] Chee Leng Lay,[a,b] Yih Hong Lee,[a] Yue-E Miao, [c] Tianxi Liu,*[c] In Yee Phang*[b] and Xing Yi Ling [c] *[a]

Nanoporous gold (NPG) promises efficient light-to-heat transformation, yet suffers limited photothermal conversion efficiency owing to the difficulty in controlling its morphology for the direct modulation of thermo-plasmonic properties. Herein, we showcase a series of shape-controlled NPG nanoparticles with distinct bowl- (NPG-B), tube- (NPG-T) and plate-like (NPG-P) structures for quantitative temperature regulation up to 140 °C in <1 s using laser irradiation. Notably, NPG-B exhibits the highest photothermal efficiency of 68%, which is >12 and 39 percentage points better than those of other NPG shapes (NPG-T, 56%; NPG-P, 49%) and Au nanoparticles (29%), respectively. We attribute NPG-B's superior photothermal performance to its >13% enhanced light absorption cross-section compared to other Au nanostructures. We further realize an ultrasensitive heat-mediated light-to-mechanical "kill switch" by integrating NPG-B with a heat-responsive shape-memory polymer (SMP/NPG-B). This SMP/NPG-B hybrid is analogous to a photo-triggered mechanical arm, and can be activated swiftly in <4 s simply by remote laser irradiation. Achieving remotely-activated "kill switch" is critical in case of emergencies such as gas leaks, where physical access is usually prohibited or dangerous. Our work offers valuable insights into the structural design of NPG for optimal light-to-heat conversion, and creates opportunities to formulate next-generation smart materials for on-demand and multi-directional responsiveness.

## Introduction

Nanoporous golds (NPGs) are highly porous structures comprising dense three-dimensional networks of interconnected and highly-curved nanoscale ligaments.[1] This unique nanoscale architecture endows NPG with high specific surface areas, high-indexed catalytically-active facets, and excellent electrical/thermal conductivity.[2–4] More importantly, NPG exhibits impressive photothermal capabilities. As a plasmonic material, gold (Au) ligaments in NPG support localized surface

plasmon resonances (LSPRs) upon light irradiation. The subsequent non-radiative decay of the surface plasmons generates substantial heat,[5] which has been widely utilized for applications in light-/heat-gated controlled molecular release, *in vivo* photothermal therapy, and plasmonic- and thermo-catalysis.[6–12] However, current NPGs suffer from a relatively low light-to-heat conversion efficiency of <60%. This limitation primarily arises from the use of a dealloying technique to generate two-dimensional NPG sheets that lack morphological control.[13] We hypothesize that attaining morphological control over NPG is critical in achieving breakthroughs in the photothermal performance of NPGs.[5] This is because such morphological control will enable the modulation of both LSPRs of NPGs and the light–matter interactions between nanoscale ligaments and the overall NPG morphology.[14] The morphological control of NPG structures is therefore key to allow heat generation at high efficiency, even at low laser irradiation powers. This capability is critical for efficient light harvesting and ultrasensitive heat-mediated actuation.

Herein, we present the first series of shape-controlled freestanding NPG nanoparticles, evaluate their morphology-dependent NPG photothermal capability, and demonstrate the use

[a]*Division of Chemistry and Biological Chemistry, School of Physical and Mathematical Sciences, Nanyang Technological University, 21 Nanyang Link, Singapore 637371. E-mail: xyling@ntu.edu.sg*

[b]*Institute of Materials Research and Engineering, Agency for Science, Technology and Research (A\*STAR), 2 Fusionopolis Way, Innovis, #08-03, Singapore 138634. E-mail: phangiy@imre.a-star.edu.sg*

[c]*State Key Laboratory for Modification of Chemical Fibers and Polymer Materials, College of Materials Science and Engineering, Donghua University, Shanghai 201620, P.R. China. E-mail: txliu@dhu.edu.cn*

†Electronic supplementary information (ESI) available. See DOI: 10.1039/c8nr04053b

‡These authors contributed equally.

of NPG as an efficient heat-responsive 'kill switch'. Using a seed-templated wet-chemical approach, we first synthesize three different shape-controlled NPG nanoparticles in high yields, including nanoporous gold bowls (NPG-B), nanoporous gold tubes (NPG-T), and nanoporous gold hexagonal plates (NPG-P). Next, we unravel the relationship between the NPG morphology and its photothermal effect using an infrared (IR) camera, which enables spatially-resolved and real-time temperature readout. We establish NPG-B as the best-performing morphology with a light-to-heat conversion efficiency approaching 70%. As a proof-of-concept application, we integrate NPG-B with a heat-responsive polymer to create a remote heat-mediated light-to-mechanical "kill switch" with swift responsiveness. This device serves as a potential early-warning/trigger system, especially in situations where physical access is prohibited. Our insights into NPG's shape-dependent photothermal effects establish the importance of the NPG structural design for optimal light-to-heat conversion, as well as pave the way for the formulation of next-generation, multi-stimuli-responsive smart materials for spatially-precise actuation.

## Experimental

### Materials

Silver nitrate (AgNO$_3$; ≥99%), hydroquinone (Hq; ≥99%), gold(III) chloride trihydrate (HAuCl$_4$; ≥99.9%), ethylene glycol (EG) and poly(vinylpyrrolidone) (PVP, average $M_w$ = 1 300 000) were purchased from Sigma Aldrich. Potassium hydroxide and hydrochloric acid (37%) were purchased from Schedelco. Nitric acid (69%) was purchased from Honeywell. Ammonium hydroxide (25% in water) was purchased from Merck. Ethanol and N,N-dimethylmethanamide (DMF) were purchased from Fisher Chemical. The polyurethane shape memory polymer (SMP MM-3520) was purchased from SMP Technologies Inc. The chemicals were used without further purification. Milli-Q water (18.2 MΩ cm$^{-1}$) was purified with a Sartorius arium® 611 UV ultrapure water system.

### Synthesis of AgCl nanocubes, AgCl nanowires and AgBr nanoplates

AgCl nanocubes were prepared using the following method. 0.4 g PVP and 0.4 g AgNO$_3$ were dissolved in 30 mL and 20 mL of cold EG, respectively. After mixing the PVP solution and AgNO$_3$ solution in a flask for 1 min at 500 rpm at room temperature, 1.23 mL of 37% HCl was added into the solution and kept stirring for 1 min. Then the solution was heated to 150 °C and kept stirring at 500 rpm for 20 min. After the reaction, the solution was naturally cooled down. 40 mL acetone was added to 10 mL of the resulting solution for sedimentation and centrifuged at 5000 rpm. After washing with water twice, the product was dispersed in 10 mL water to obtain a white suspension. This white suspension was used for future reactions. AgCl nanowires were synthesized using the method reported by Bi et al.[15] AgBr hexagonal nanoplates were prepared using the method reported by Wang et al.[16]

### Synthesis of nanoporous gold (NPG)

0.35 g PVP was dissolved in 50 mL water. 300 mg Hq was dissolved in 10 mL water. HAuCl$_4$ was also dissolved in water to obtain a 0.5 M solution. AgCl nanocube solution (containing 51 mg AgCl) was first mixed with 45 mL PVP solution at 1300 rpm in RBF. After mixing for 1 min, 780 μL Hq solution was added followed by the addition of 323 μL HAuCl$_4$ solution. After reaction for 1 min at 1300 rpm at room temperature, the AgCl/NPG-B hybrid was obtained. The solution was centrifuged at 3000 rpm for 3 min and washed twice with water. The product could be re-dispersed in water. After mixing the AgCl/NPG-B hybrid solution with 10 mL ammonia, the solution was centrifuged at 3000 rpm for 3 min and washed with water twice. The as-synthesized nanoporous gold bowl (NPG-B) was then re-dispersed in water. The concentration of the NPG-B solution was determined by inductively coupled plasma optical emission spectrometry (ICP-OES). Nanoporous gold tubes (NPG-T) and nanoporous gold plates (NPG-P) were synthesized using a similar method, except that AgCl nanowires and AgBr nanoplates were used as sacrificial templates.

### Synthesis of Au NPs, smooth Au plates, Ag nanocubes and Ag octahedral

Au NPs with the same size as NPG ligaments were prepared by following the synthetic strategy reported by Sivaraman et al.[17] Smooth Au plates were prepared using the method reported by Jiu et al.[18] Ag nanocubes and Ag octahedral were prepared by following the experimental procedures reported by Yang et al. and Lee et al.[19,20]

### Photothermal temperature characterization

Using NPG-B as an example, we manually dropcasted its colloidal solution onto a thin layer chromatography (TLC) plate to form a particle cluster with a regulated area density of ~7.55 μg mm$^{-2}$ (diameter ~ 4 mm). Other NPG samples were prepared with the same area density. The actual area density of all NPG particles dropcasted on the substrate was confirmed by ICP-OES. The photothermal temperature under 532 nm laser irradiation (25 to 90 mW, power tuned by ND filters) was evaluated using an FLIR SC7000 infrared (IR) camera to track real-time and spatially-resolved photothermal temperature profiles.

### Preparation of shape memory polymer (SMP)/NPG-B

Typically, 500 mg of SMP pellets were dissolved in 15 mL DMF at 90 °C. The solution was poured into a glass Petri dish. The solvent was slowly evaporated at 70 °C for 24 h to obtain an SMP film. SMP was cut into 5 × 2 mm strips with a thickness of 0.05 mm and NPG-B was dropcasted onto SMP. The area density of NPG-B on SMP was controlled to be the same as those previously prepared on TLC substrates.

### Materials characterization

Nanoparticles were dropcasted onto a clean silicon substrate for scanning electron microscopy (SEM) observation. SEM

imaging was performed using a JEOL JSM 7600F microscope. The voltage was set at 5 kV. X-ray photoelectron spectroscopy (XPS) spectra were obtained using a Phoibos 100 spectrometer with a monochromatic Mg X-ray radiation source. The C 1s binding energy peak at 284.5 eV is used for XPS calibration. The composition and concentration analysis of the obtained nanoparticle suspension was conducted using a Thermo Scientific iCAP 6500 model ICP-OES. The nanoparticle suspension was mixed with aqua regia, and then diluted with water prior to ICP-OES measurement. $X$–$z$ Raman imaging was performed using a Ramantouch microspectrometer (Nanophoton Inc., Osaka, Japan) with an excitation wavelength of 532 nm. A 532 nm laser (power density of 6.25 mW mm$^{-2}$) attached to an uRaman microscope was used for controlling the movement of SMP/NPG-B. The movement of SMP/NPG-B was recorded in the form of a video and frames at pre-defined timings were analyzed using the ImageJ software.

## Results and discussion

Shape-controlled synthesis of NPG offers a great opportunity to tailor its shape-dependent thermo-plasmonic properties essential for enhanced photothermal performance (Fig. 1A). To achieve this, we employ a two-step template-assisted method that involves an initial growth of NPG on shape-controlled Ag halide-based sacrificial templates (including AgCl nanocubes, AgCl wires and AgBr nanoplates; Fig. S1†).[21] This is followed by the ammonia-based etching of Ag halide sacrificial templates to yield uniform NPGs with bowl-, tube-, and plate-like shapes that are denoted as NPG-B, NPG-T and NPG-P, respectively (Fig. 1B–D; Fig. S1†). All NPG structures comprise uniform interconnected ligaments with a size of ~18 ± 2 nm, and small pores with sizes ranging from 4–30 nm (Fig. S2†). More importantly, the morphologies of all as-synthesized NPG structures are distinct and predominantly defined by the shapes of their respective sacrificial templates. NPG-B features a hemispherical bowl-like shape with an open cavity of 0.7 ± 0.1 μm diameter (Fig. 1B). NPG-T has a hollow tube-like structure (length, 6.1 ± 2.3 μm) with open ends on both sides and an inner diameter of 0.2 ± 0.1 μm (Fig. 1C; Fig. S3A†). NPG-P displays a hexagonal and hollow plate-like structure with close ends on all sides (edge length, 2.0 ± 0.5 μm) and an average thickness of 0.5 ± 0.1 μm (Fig. 1D; Fig. S3B†). We attribute the presence of the open cavity and the hollow structure in our NPGs to the removal of the inner Ag-based sacrificial templates after the growth of NPG on these templates.

Chemical composition analyses of NPGs using X-ray photoelectron spectroscopy (XPS) and energy dispersive X-ray spectroscopy (EDS) demonstrate the successful reduction of Au(III) to Au(0), as well as the significant removal (≥94%) of the Ag-based sacrificial template (Fig. S4 and S5†). Further quantitative elemental analysis using inductively-coupled plasma optical emission spectrometry (ICP-OES) affirms the negligible residual Ag present (<6%) in all three NPG morphologies
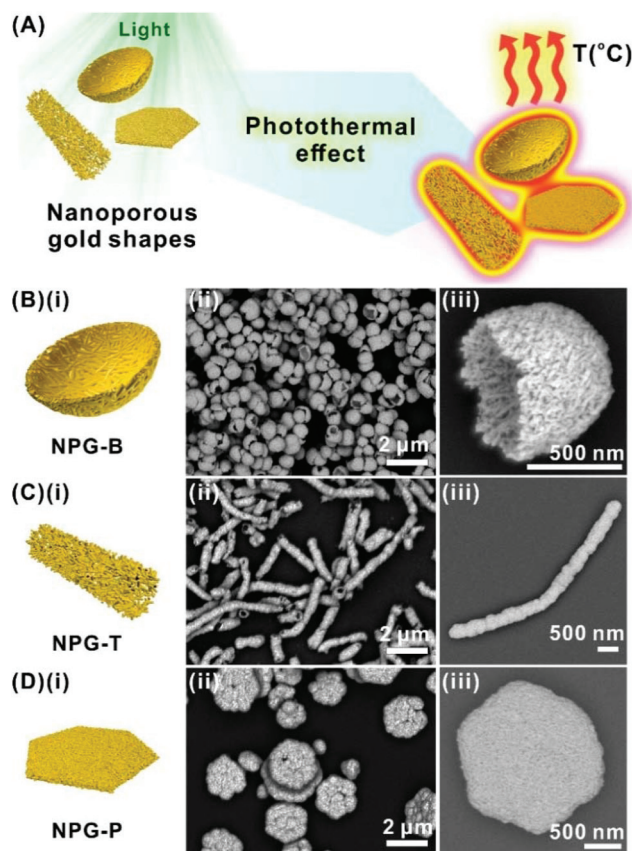


Fig. 1  Characterization of the as-synthesized nanoporous gold (NPG) nanoparticles with various shapes. (A) Scheme depicting the use of various shape-controlled NPGs for light-to-heat conversion. (B–D) As-synthesized nanoporous gold bowl (NPG-B), nanoporous gold tube (NPG-T) and nanoporous gold plate (NPG-P), respectively. (i) Schemes, (ii) SEM images and (iii) magnified SEM images of the respective NPG particles.

(Table S1†). We also note that all NPGs exhibit a broadband extinction spectrum between 400–1000 nm, whereas 18 nm Au nanoparticles (comparable to NPG's ligament sizes) exhibit LSPR only at 520 nm (Fig. S6 and S7†). The differences in the extinction spectra are attributed to the strong plasmonic coupling between interconnected Au nanosized ligaments within the nanoporous framework architecture.[22,23] Collectively, these results highlight the first synthesis of shape-controlled NPG structures, which are crucial for the subsequent investigation of their shape-dependent photothermal performances.

We evaluate the remote and on-demand photothermal heating of NPG (532 nm, 90 mW) by employing an infrared (IR) camera to monitor its real-time and spatially-resolved temperature profiles during laser irradiation (Fig. 2A). Using NPG-B as an example, we deposit the particles onto a thin layer chromatography (TLC) plate to form a particle cluster with a constant area density of ~7.55 μg mm$^{-2}$ (diameter ~ 4 mm) and a thickness estimated at ~17 layers of NPG-B (Fig. S8 and S9†). The NPG-B cluster exhibits a homogeneous surface temperature of 25 °C prior to laser illumination
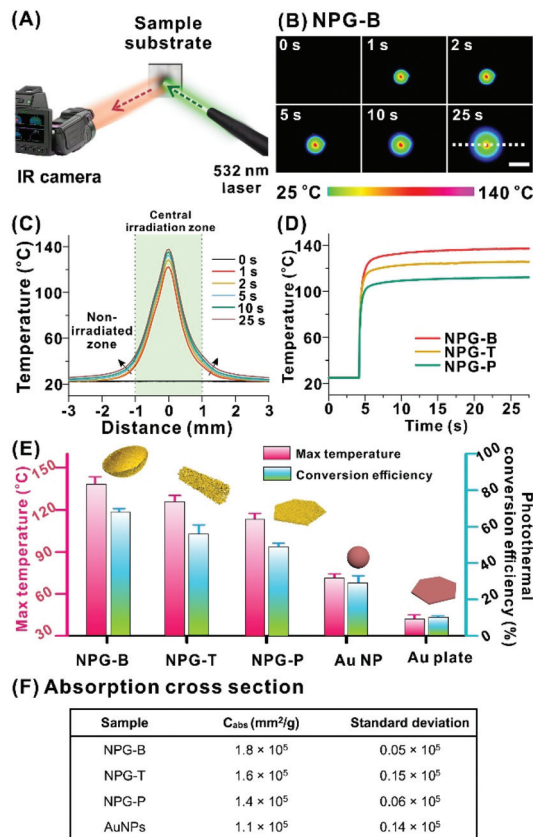
**Fig. 2** Photothermal effect of various shape-controlled NPGs. (A) Scheme of a photothermal experimental setup composed of a laser beam irradiating on the NPG surface and an IR camera to record the spatial temperature profile of the irradiated NPG in real time. (B) Thermogram of NPG-B upon laser irradiation. Laser power = 90 mW. Scale bar, 4 mm. (C) Spatial temperature profiles of NPG-B as indicated in (B). (D) Time–temperature profiles of various NPG shapes upon laser irradiation. (E) Maximum equilibrium temperature and photothermal conversion efficiency of various metal nanostructures. Au NP denotes gold nanoparticle. (F) Absorption cross-section of NPG-B, NPG-T, NPG-P, and AuNPs.

(Fig. 2B, 0 s). Upon laser irradiation, the surface temperature of NPG-B at the central irradiation zone (distance from the irradiation center, $x = 0$ mm) rapidly increases to ~122 °C at a maximum heating rate $((\mathrm{d}T/\mathrm{d}t)_{\max})$ of ~364 °C s$^{-1}$ (Fig. S10†), which eventually plateaus at ~138 °C beyond 10 s (Fig. 2C and D). The spatial-temperature plots exhibit Gaussian-like profiles, indicating localized photothermal heating due to the use of a Gaussian laser beam. The temporal temperature profile indicates that the photothermal heating of NPG-B occurs in two sequential steps.[24] First, there is an initial surge in the surface temperature at the central irradiated zone due to the instantaneous photothermalization of light by NPG-B. A gradual temperature increment to a steady state follows this initial surge, indicating that a thermal equilibrium is achieved between photothermal heat generation and heat dissipation to the entire NPG-B cluster (even the non-irradiated zone), the underlying silica layer, and the surrounding air environment.

Similarly, we also observe a two-step cooling process when the laser irradiation is switched off, whereby the surface temperature rapidly decreases from 138 to 33 °C within 1 s and later equilibrates at ~25 °C within 25 s (Fig. S11†). More importantly, NPG-B exhibits a >2-fold higher maximum equilibrium temperature and heating rate as compared to a control platform comprising 18 nm Au nanoparticles (similar to NPG-B's ligament sizes, surface temperature, 68 °C; maximum heating rate, 140 °C s$^{-1}$; Fig. S12†). This highlights the importance of constructing interconnected Au ligaments in a NPG architecture to attain photothermal heating beyond conventional randomly-aggregated Au nanoparticle platforms (to be discussed later).

Next, we demonstrate the shape dependence of NPG's photothermal effect by comparing the light-to-heat conversion efficiencies of various NPG shapes (NPG-B, NPG-T and NPG-P) under identical experimental conditions. Similar to NPG-B, both NPG-T and NPG-P display a two-step photothermal heating phenomenon where the surface temperature first surges and eventually reaches a thermal equilibrium (Fig. 2D). Notably, the maximum surface temperature attained for NPG-T (125 °C) and NPG-P (112 °C) is at least 13 °C lower than that for NPG-B (138 °C; Fig. 2D and E; Fig. S13†). The $(\mathrm{d}T/\mathrm{d}t)_{\max}$ values of NPG-T and NPG-P are ~343 °C s$^{-1}$ and 301 °C s$^{-1}$, respectively, which are at least 21 °C s$^{-1}$ slower than that of NPG-B (Fig. S14A†). More importantly, NPG-B exhibits the highest photothermal efficiency – defined as the ratio of the heat energy output and the laser energy input – of ~68% (Fig. 2E) and is at least 12% higher than those of NPG-T (56%) and NPG-P (49%; ESI Notes 1; Fig. S15; Table S2†). We also affirm the importance of NPG's unique framework to achieve better light-to-heat conversion by comparing against their smooth counterparts and Au nanoparticles. Using nanoplates as an example, NPG-P exhibits ~5-fold and 2-fold better photothermal conversion efficiency than smooth Au nanoplates (49% vs. 10%; Fig. S16†) and randomly-aggregated Au nanoparticles (29%; Fig. S17†), respectively. Collectively, NPG-B's superior photothermal efficiency, maximum achievable equilibrium temperature and heating rate over those of NPG-T and NPG-P platforms clearly underscore the impact of NPG's morphology on their corresponding photothermal performances.

We attribute the superior photothermal performance of NPG-B to its highest absorption cross-section ($C_{\mathrm{abs}}$; mm$^2$ g$^{-1}$) as compared to NPG-T and NPG-P. The $C_{\mathrm{abs}}$ is associated with the heat generation ability of plasmonic nanoparticles (Fig. 2F; refer to ESI Notes 2; Fig. S18†).[25] From the photothermal heat generated, we calculate the absorption cross-section of various shape-controlled NPG particles using the following equation:[25]

$$C_{\mathrm{abs}} = Q/(d \times N \times P \times \Delta t) \tag{1}$$

where $Q$ is the heat generated from photothermal conversion (J), $d$ is the penetration depth of the laser beam into the particle cluster (mm), $N$ is the apparent density of NPG (g mm$^{-3}$), $P$ is the laser power (W), and $\Delta t$ is the duration of laser irradiation (s). Notably, this method gives a more accurate esti-

mation of the $C_{abs}$ because our NPG particles deviate from the typical Mie and Beer–Lambert law due to the presence of scattering particles and particle–particle (ligament–ligament) interactions.[26,27]

NPG-B exhibits the highest $C_{abs}$ of ~1.8 × 10⁵ mm² g⁻¹ (Fig. 2F), which is >13%, 29% and 64% higher than those of NPG-T (1.6 × 10⁵ mm² g⁻¹), NPG-P (1.4 × 10⁵ mm² g⁻¹) and Au nanoparticles (1.1 × 10⁵ mm² g⁻¹), respectively. We normalize $C_{abs}$ against the Au mass because it quantitatively compares and highlights the enhanced photothermal effect arising solely from NPG's geometry, especially when all NPGs possess a similar ligament size in our experiments. We also validate the $C_{abs}$ of Au nanoparticles in this work with theoretical prediction and experimental results from the previous literature (refer to ESI Notes 2†).[25] Considering that all NPGs possess similarly-sized Au ligaments (~18 nm), we then assume that the absorption property of an individual Au ligament is similar and any differences in NPG's absorption cross-sections are mainly attributed to the variation in its morphology. Consequently, NPG-B's enhanced absorption cross-section likely stems from its symmetry-broken bowl-shape geometry, which allows strong plasmonic coupling between dipolar plasmons from the cavity (the aperture hole) and dipolar/quadrupolar plasmons from the NPG's shell.[28,29] Such plasmon hybridization has been reported to induce significant charge accumulation at the bowl edges for immense and spatially-localized electric field enhancement.[30] Hence, our results clearly indicate that the combination of the geometry-induced optical phenomenon through the synthesis of shape-controlled NPG structures and the extensive plasmonic coupling between ligaments within the unique 3D bowl-like structure is critical in enhancing the light harvesting effects. As for the other NPGs (NPG-T and NPG-P), we note that NPG-T has higher $C_{abs}$ and photothermal efficiency compared to NPG-P, which are likely ascribed to the plasmonic coupling across the intraparticle gap within the hollow tube-like structure. Collectively, our findings emphasize the importance of NPG's morphological design to attain efficient light-to-heat transformation. This is critical to realize drastic and instantaneous temperature changes even at low laser irradiation power, which is essential for photothermal applications, such as *in vivo* photothermal therapy, light-to-heat harvesting and heat-mediated actuation.

Using our best-performing NPG-B, we further demonstrate its photothermal capability to achieve quantitative and rapid temperature control. By controlling the laser power between 25 and 90 mW, we systematically elevate the surface temperature of NPG-B from 33 to 138 °C (Fig. 3A), respectively, with a similar two-step heating profile. Switching off the laser leads to a decrease in the surface temperatures of all NPG-B to the pre-heated state of ~25 °C (Fig. 3B). Correspondingly, regulating the laser power from 25 mW to 90 mW allows a dynamic modulation of both the maximum heating speed and cooling speed from 31 °C s⁻¹ to >350 °C s⁻¹ (Fig. 3C and D; Fig. S19†). The changes in the surface temperature ($\Delta T$) in both heating and cooling processes are proportional to the laser power (Fig. 3E), indicating that the NPG's surface temperature can be
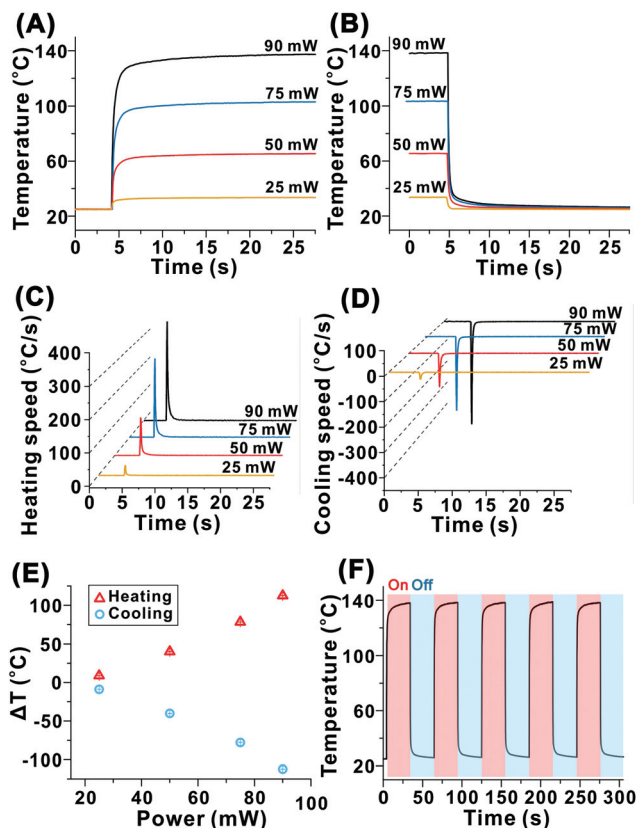


Fig. 3 Laser power-dependent photothermal properties of NPG-B. (A, B) Temperature−time profiles of NPG-B when the laser irradiation is switched on and off, respectively. The applied laser power is controlled between 25 and 90 mW. (C) Heating and (D) cooling speed of NPG-B upon irradiation with different laser powers. (E) Changes in the surface temperature of NPG-B as a function of laser power during heating and cooling. (F) Heat−cool cycling test on NPG-B (laser power = 90 mW).

precisely programmed simply *via* the laser power applied. Moreover, NPG-B also demonstrates timely and reproducible photothermal heating where its surface temperature alternates precisely between 25 °C and 138 °C over five cycles of successive photothermal heating/cooling (laser power = 90 mW; Fig. 3F). This ability to achieve on-demand and programmable temperature control suggests the potential application of NPG-B in diverse thermal mechanical applications.

By integrating NPG-B's superior photothermal performance with a thermo-responsive shape-memory polymer (SMP; Fig. 4A), we further create a photo-triggered mechanical arm as a fast-response and remote "kill-switch". This proof-of-concept application exploits the photothermal heat generated from NPG to trigger the polymer chain movement to relieve the stress accumulated in a pre-deformed SMP,[31] thus reverting the heat-responsive material to its original shape. In a typical set-up, one side of a SMP strip is first loaded with NPG-B particles *via* repeated drop-casting. The SMP/NPG-B ensemble is subsequently folded at an angle of ~30° using a reported protocol to instill the memory of the polymer at a temperature lower than its glass transition temperature ($T_g$, 35 °C).
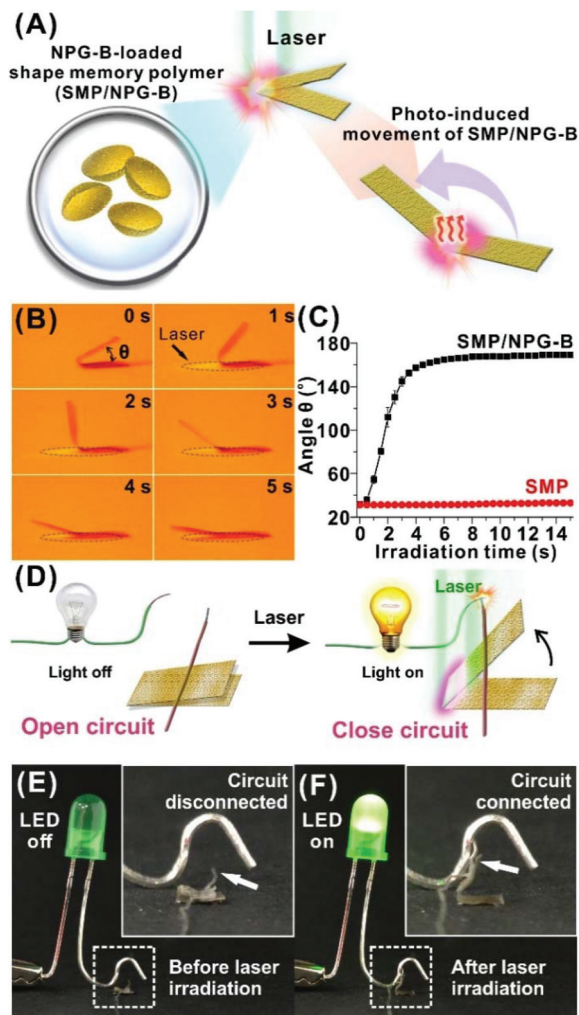
Fig. 4 Integration of NPG with the shape memory polymer (SMP/NPG-B) for application as a heat-mediated light-to-motion transducer. (A) Scheme illustrating remote heat-mediated light-to-motion conversion using a shape-memory polymer (SMP) strip that is decorated with NPG-B. (B) Photographic images displaying the time-dependent movement of a SMP/NPG-B strip upon laser irradiation. The black circles indicate the area under laser irradiation. θ represents the opening angle of folded SMP. (C) Plots of the opening angle of folded SMP/NPG-B against laser irradiation time. The SMP strip in the absence of NPG-B coatings under laser irradiation is also included for comparison. (D) Scheme depicting the integration of SMP/NPG-B with an electrical circuit for the realization of an efficient remote laser-controlled "kill switch" to activate the LED light which mimics an alarm/early-response system. (E and F) Experimental realization of a light-triggered, heat-mediated "kill switch" using SMP/NPG-B before and after laser irradiation, respectively. The insets show the corresponding zoom-in images of the SMP/NPG-B "kill switch" installed in the system.

Illuminating the pre-folded region (laser power = 100 mW) rapidly reverts the SMP/NPG-B strip to its original position by opening up with an angle change from 32° to 169° within a short duration of 4 s (Fig. 4B and C). In contrast, the SMP strip without NPG-B exhibits negligible movement (<2°) upon laser irradiation, affirming that the drastic movement in SMP/NPG-B is caused by photothermal heating and not due to

laser-induced processes and/or potential heating from the laser source. We also note that the SMP/NPG-B strip did not completely revert to its initial state (180°) possibly due to the partial disruption of the cross-linking points present in the original SMP during intense photothermal heating.[31] Furthermore, we observe that the heat-induced mechanical behavior in SMP/NPG-B (≤4 s) is slightly sluggish compared to the photothermal heating in NPG-B (≤1 s). This is due to the relatively slower heat-triggered recovery of SMP, which typically occurs in a time-scale between seconds and minutes.[32] Nevertheless, the response time in our SMP/NPG-B is >40-fold faster compared to similar SMP systems such as 3D printed polyurethane.[31] We attribute this phenomenon to NPG-B's intense and localized photothermal heating which enables timely and spatially-controlled mechanical movement directly at the point of interest. This effectively overcomes the slow responses and energy wastage commonly encountered in traditional heating methods (such as an oven or heat-plate), where the latter requires gradual ramping to the target temperature and is unable to achieve localized and remote heating. It is also noteworthy that our free-standing NPGs allow seamless integration with thermo-sensitive SMP as well as transfer onto arbitrary surfaces, whereas conventional NPG platforms involve 2D or surface-bound particles that cannot be easily transferred.[33]

Building on our SMP/NPG-B system, we further devise a highly responsive photo-triggered switch to serve as an alarm device and/or "kill-switch" with potential application in the remote enforcement of automated safety countermeasures. This is important in the event of an emergency, especially when access to safety controls is dangerous or restricted. As a proof-of-concept, we integrate our SMP/NPG-B as a photo-responsive mechanical switch to remotely activate a LED light that mimics an alarm system (Fig. 4D). Prior to laser irradiation, the angle of the strip is 0° and the LED light is off because the electrical circuit is open (Fig. 4E). When we direct the laser irradiation onto the SMP/NPG-B strip, the photo-triggered switch rapidly turns on (opening angle = 60°; Fig. 4F) and activates the LED-based "alarm system" within 2 s of laser irradiation. These results jointly demonstrate SMP/NPG-B as an ideal strategy to design an ultrasensitive mechanical switch energized by light-to-heat-to-motion conversion. This strategy is highly relevant in situations requiring swift and remote control and where physical access is prohibited such as in confined spaces with gas leakage. The ensemble of benefits offered in our design also creates new possibilities for the development of next-generation hybrid smart materials to achieve multi-stimuli-responsive and multi-directional actuation that can be remotely directed simply using laser irradiation.

## Conclusions

In this work, we develop three distinct NPG nanoparticles with bowl-, tube- and plate-like structures to enable highly sensitive

and quantitative temperature control up to 140 °C in <1 s. Direct evaluation of the photothermal conversion efficiencies unveils bowl-like NPG (NPG-B; 68%) as the best performing NPG, which is at least 2-fold superior to conventional Au nanoparticles. These results highlight the importance of constructing the NPG framework and modulating the NPG's shape-dependent thermo-plasmonic effect at the nanoscale in achieving efficient light-to-heat conversion. By integrating NPG-B with a heat-responsive polymer, we further devise a heat-mediated light-to-mechanical "kill switch" that can be remotely and swiftly activated in <4 s using laser irradiation. This "kill switch" will be especially crucial in emergency situations such as during gas leaks or natural disasters, where physical access to conventional alert systems is typically prohibited or dangerous. Our work offers valuable insights into the structural design of NPG for optimal light-to-heat conversion, as well as creates immense opportunities in the formulation of next-generation smart materials for on-demand and multi-directional responsiveness.

## Conflicts of interest

There are no conflicts to declare.

## Author contributions

Z. Y., X. H., H. K. L. and X. Y. L. conceived and designed the research. Z. Y., X. H., G. C. P. Q., C. S. L. K., C. L. L., and I. Y. P. carried out the experiments. Z. Y., X. H., H. K. L., Y. H. L., Y. M., I. Y. P. and X. Y. L. analysed the results and wrote the manuscript in consultation with T. L. All authors provided critical feedback and helped shape the manuscript. T. L., I. Y. P., and X. Y. L. supervised the project.

## Acknowledgements

## References

1  A. Wittstock, V. Zielasek, J. Biener, C. Friend and M. Bäumer, *Science*, 2010, **327**, 319–322.

2  Y. Deng, Y. Cai, Z. Sun, J. Liu, C. Liu, J. Wei, W. Li, C. Liu, Y. Wang and D. Zhao, *J. Am. Chem. Soc.*, 2010, **132**, 8466–8473.

3  C. Li, Ö. Dag, T. D. Dao, T. Nagao, Y. Sakamoto, T. Kimura, O. Terasaki and Y. Yamauchi, *Nat. Commun.*, 2015, **6**, 6608.

4  S. Pedireddy, H. K. Lee, W. W. Tjiu, I. Y. Phang, H. R. Tan, S. Q. Chua, C. Troadec and X. Y. Ling, *Nat. Commun.*, 2014, **5**, 4947.

5  H. Chen, L. Shao, T. Ming, Z. Sun, C. Zhao, B. Yang and J. Wang, *Small*, 2010, **6**, 2272–2280.

6  V. Voliani, G. Signore, O. Vittorio, P. Faraci, S. Luin, J. Peréz-Prieto and F. Beltram, *J. Mater. Chem. B*, 2013, **1**, 4225–4230.

7  R. Jiang, B. Li, C. Fang and J. Wang, *Adv. Mater.*, 2014, **26**, 5274–5309.

8  G. M. Santos, F. Zhao, J. Zeng and W.-C. Shih, *Nanoscale*, 2014, **6**, 5718–5724.

9  H.-W. Chen, C.-Y. Hong, C.-W. Kung, C.-Y. Mou, K. C.-W. Wu and K.-C. Ho, *J. Power Sources*, 2015, **288**, 221–228.

10  Z. Bai, X. Ren, Z. Gong, C. Hao, Y. Chen, P. Wan and X. Meng, *Chin. Chem. Lett.*, 2017, **28**, 1901–1904.

11  H.-D. Cui, D.-H. Hu, J.-N. Zhang, G.-H. Gao, C.-F. Zheng, P. Gong, X.-H. Xi, Z.-H. Sheng and L.-T. Cai, *Chin. Chem. Lett.*, 2017, **28**, 1391–1398.

12  J. Wang, S. Mao, H.-F. Li and J.-M. Lin, *Anal. Chim. Acta*, 2018, **1027**, 76–82.

13  Y. Yamauchi, A. Tonegawa, M. Komatsu, H. Wang, L. Wang, Y. Nemoto, N. Suzuki and K. Kuroda, *J. Am. Chem. Soc.*, 2012, **134**, 5100–5109.

14  Y. Shen, J. Zhou, T. Liu, Y. Tao, R. Jiang, M. Liu, G. Xiao, J. Zhu, Z.-K. Zhou and X. Wang, *Nat. Commun.*, 2013, **4**, 2381.

15  Y. Bi and J. Ye, *Chem. Commun.*, 2009, 6551–6553.

16  H. Wang, Y. Liu, P. Hu, L. He, J. Li and L. Guo, *ChemCatChem*, 2013, **5**, 1426–1430.

17  S. K. Sivaraman, S. Kumar and V. Santhanam, *J. Colloid Interface Sci.*, 2011, **361**, 543–547.

18  J. Jiu, K. Suganuma and M. Nogi, *J. Mater. Sci.*, 2011, **46**, 4964–4970.

19  Y. H. Lee, W. Shi, H. K. Lee, R. Jiang, I. Y. Phang, Y. Cui, L. Isa, Y. Yang, J. Wang and S. Li, *Nat. Commun.*, 2015, **6**, 6990.

20  Y. Yang, Y. H. Lee, I. Y. Phang, R. Jiang, H. Y. F. Sim, J. Wang and X. Y. Ling, *Nano Lett.*, 2016, **16**, 3872–3878.

21  Z. Yang, S. Pedireddy, H. K. Lee, Y. Liu, W. W. Tjiu, I. Y. Phang and X. Y. Ling, *Chem. Mater.*, 2016, **28**, 5080–5086.

22  L. Guo, J. A. Jackman, H.-H. Yang, P. Chen, N.-J. Cho and D.-H. Kim, *Nano Today*, 2015, **10**, 213–239.

23  F. Zhao, J. Zeng and W.-C. Shih, *Sensors*, 2017, **17**, E1519.

24  W. Gao, H. K. Lee, J. Hobley, T. Liu, I. Y. Phang and X. Y. Ling, *Angew. Chem., Int. Ed.*, 2015, **54**, 3993–3996.

25  Z. Qin, Y. Wang, J. Randrianalisoa, V. Raeesi, W. C. W. Chan, W. Lipiński and J. C. Bischof, *Sci. Rep.*, 2016, **6**, 29836.

26  L. V. Besteiro, K. Gungor, H. V. Demir and A. O. Govorov, *J. Phys. Chem. C*, 2017, **121**, 2987–2997.

27  J. R. Dunklin and D. K. Roper, *J. Nanomater.*, 2017, **2017**, 9.

28 J. Ye, L. Lagae, G. Maes, G. Borghs and P. Van Dorpe, *Opt. Express*, 2009, **17**, 23765–23771.

29 J. Ye, N. Verellen, W. Van Roy, L. Lagae, G. Maes, G. Borghs and P. Van Dorpe, *ACS Nano*, 2010, **4**, 1457–1464.

30 P. Van Dorpe and J. Ye, *ACS Nano*, 2011, **5**, 6774–6778.

31 H. Yang, W. R. Leow, T. Wang, J. Wang, J. Yu, K. He, D. Qi, C. Wan and X. Chen, *Adv. Mater.*, 2017, **29**, 1701627.

32 C. Liu, H. Qin and P. T. Mather, *J. Mater. Chem.*, 2007, **17**, 1543–1558.

33 D. Wang and P. Schaaf, *J. Mater. Chem. B*, 2012, **22**, 5344–5348.